Mechanical stimulation of a bioactive, functionalized PVDF-TrFE scaffold provides electrical signaling for nerve repair applications

Jacob A. Orkwis [a], Ann K. Wolf [b], Zachary J. Mularczyk [c], Andrew E. Bryan [a], Corinne S. Smith [a], Ryan Brown [a], Maksym Krutko [c], Adam McCann [d], Ryan M. Collar [d], Leyla Esfandiari [b,c,e], Greg M. Harris [a,c,f,*]

[a] Department of Chemical and Environmental Engineering, University of Cincinnati, Cincinnati, OH 45221, United States of America
[b] Department of Electrical Engineering and Computer Science, University of Cincinnati, Cincinnati, OH 45221, United States of America
[c] Department of Biomedical Engineering, University of Cincinnati, Cincinnati, OH 45221, United States of America
[d] Department of Otolaryngology-Head & Neck Surgery, University of Cincinnati College of Medicine, Cincinnati, OH 45267, United States of America
[e] Department of Environmental and Public Health Sciences, University of Cincinnati, Cincinnati, OH 45267, United States of America
[f] Neuroscience Graduate Program, University of Cincinnati College of Medicine, Cincinnati, OH 45267, United States of America

ARTICLE INFO

ABSTRACT

Traumatic nerve injuries have limited success in achieving full functional recovery, with current clinical solutions often including implementation of nerve grafts or the use of nerve conduits to guide damaged axons across injury gaps. In search of alternative, and complimentary solutions, piezoelectric biomaterials demonstrate immense potential for tissue engineering applications. Piezoelectric poly(vinylidene fluoride-triflouroethylene) (PVFD-TrFE) scaffolds can be harnessed to non-invasively stimulate and direct function of key peripheral nervous system (PNS) cells in regeneration strategies. In this study, electrospun PVDF-TrFE was characterized, fabricated into a 3D scaffold, and finally rendered bioactive with the incorporation of a cell-secreted, decellularized extracellular matrix (dECM). PVDF-TrFE scaffolds were characterized extensively for piezoelectric capacity, mechanical properties, and cell-material interactions with fibroblasts and Schwann cells. Through functionalization of PVDF-TrFE scaffolds with a native, cell-assembled dECM, the ability to promote cell adhesion and enhanced viability was also demonstrated. Additionally, incorporation of bioactive functionalization improved the assembly of key regenerative ECM proteins and regenerative growth factors. PVDF-TrFE scaffolds were then fabricated into a conduit design that retained key physical, chemical, and piezoelectric properties necessary for PNS repair. This work shows great promise for multi-cue, electrospun biomaterials for regeneration of the PNS in traumatic injury.

1. Introduction

Peripheral nervous system (PNS) damage is a frequent result of traumatic injury. Severe trauma that fails to attain functional recovery can induce a prolonged burden on the health of the individual. While the PNS has a remarkable ability to repair damage through an autologous tissue-mediated response and recovery cascade, traumatic injuries generally require clinical interventions such as nerve grafting or nerve transfers to regain functional recovery [1,2]. Many reasons exist for the lack of recovery in traumatic injury, including slow regeneration of axons over large injury gaps, loss of extracellular matrix (ECM) physical guidance cues, and lack of the proper biochemical signaling [3].

Therefore, clinicians commonly use autologous or allographic nerve grafts or guidance conduits in injury gaps to provide the proper physical and biochemical guidance to axonal growth cones. However, nerve grafts traditionally present unavoidable challenges such as donor site morbidity, lack of available tissue, and incomplete motor recovery [4]. To address the clinical need for regeneration in the PNS, the focus of engineered biomaterials has shifted to utilize the native repair functionality of the PNS to develop therapeutic alternatives to the autologous nerve graft. Therefore, multifaceted biomaterials offer promise to the advent of alternative PNS therapeutics for promoting functional recovery.

Piezoelectric materials are promising for biomaterial design due to

---

their potential to deliver on-demand, non-invasive electric signaling. For soft tissue applications such as skin, cardiac, and nervous tissue, this electric output can promote a distinctly favorable regenerative micro-environment [5–7]. Poly(vinylidene fluoride) (PVDF), and its copolymer, poly(vinylidene fluoride-trifluoroethylene) (PVDF-TrFE), are piezoelectric materials that have demonstrated preliminary success in PNS applications. This is attributed, in part, to flexibility, biocompatibility, and robust piezoelectric capacity [8]. Further, PVDF-TrFE scaffolds produced by electrospinning can mimic the physical structure of native ECM in regeneration [9]. Additionally, the potential ability to tailor and functionalize the material as seen in other applications, such as utilizing bioactive functionalization with ECM proteins that stimulate a regenerative environment capable of directing cellular function [10–12]. This bioactive functionalization can also be prepared to unlock key repair mechanisms in the PNS such as stimulation of the highly plastic Schwann cell toward a more favorable repair phenotype for regeneration across the wound space [1,13–15].

To fully harness and understand piezoelectric materials as it relates to cells and tissue, a robust understanding of the electric potential of PVDF-TrFE must be realized. It has previously been established that the application of small DC electric fields can augment the regeneration of axons, the extension of dorsal root ganglion neurites, and help mediate the plasticity of Schwann cells [16–18]. Furthermore, the ability to tailor signaling events to provide a "pro-repair" phenotype in Schwann cells and the PNS may likely be a key to unlocking the intrinsic repair potential [1,2]. However, there is limited understanding of how, specifically, the piezoelectric capacity of electrospun biomaterials can be precisely controlled to achieve specific outcomes and how to best functionalize these materials to integrate into the PNS microenvironment and direct cell behavior.

Previously, we have demonstrated the ability to electrospin PVDF-TrFE fibers and culture Schwann cells and fibroblasts in an aligned fashion on the scaffolds [8]. In this work we further establish the *in vitro* efficacy of PVDF-TrFE by systematically quantifying and analyzing the piezoelectricity of the electrospun scaffold. Furthermore, a robust 3D guidance conduit was fabricated from the individual scaffold layers for downstream *in vivo* applications. Finally, we introduce a novel approach to functionalizing PVDF-TrFE with a native, decellularized ECM (dECM) secreted from cells for enhanced bioactivity and integration into tissue, where we demonstrate no loss of piezoelectric capacity in the bioactive, modified PVDF-TrFE scaffolds. Altogether, this results in a multi-cue biomaterial capable of tailoring non-invasive and on demand physical, chemical, and electric signaling to cells and tissue to promote regeneration of the PNS while simultaneously offering insight into the capabilities of piezoelectric materials for tissue engineering applications (Fig. 1).

2. Materials and methods

2.1. Preparation of nanofiber scaffolds and conduits

PVDF-TrFE nanofiber scaffolds were prepared as described by our previous work [8]. In brief, an electrospinning solution consisting of 20 % PVDF-TrFE (70/30) (PolyK Technologies, State College, PA) and solvent of *N,N*-dimethylformamide (DMF) and acetone (6/4 v/v) was added to a 5 mL syringe fitted with a 20-gauge needle. The syringe pump was set to supply a flow rate of 1 mL h^{-1}. The needle tip was positioned 10 cm away from the collector. The collector was rotated at 2000 RPM to produce aligned fibers and wrapped in a conductive polymer liner (McMaster-Carr). A voltage of 18 kV was applied between the needle tip and the collector. To fabricate nerve guidance conduits, rectangular 20 mm wide by 180 mm long scaffolds were cut, wrapped around a 24.71 mm by 1.71 mm stainless steel mandrel, and rolled to form hollow conduit structures.

2.2. Scaffold and conduit characterization

The morphology of electrospun fibers was analyzed using scanning electron microscopy (SEM), (Apreo C SEM, Thermo Fisher). Two samples per experimental condition were prepared by sputter coating a layer of gold for approximately 10 s. An acceleration voltage of 5 kV was used with a working distance of 5 mm. ImageJ software (version 1.52p) was used to calculate average fiber diameter (n = 80).

Porosity of the resultant scaffolds was estimated by comparing the density of the electrospun scaffold ($\rho_{scaffold}$) to the unprocessed PVDF-TrFE powder (ρ_{raw}):

$$Porosity\ (\%) = \left(1 - \frac{\rho_{scaffold}}{\rho_{raw}}\right) \times 100\% \qquad (1)$$

Scaffold density was calculated by measuring geometrical dimensions and dry weight, with powder density supplied by manufacturer (1.88 g-cm^{-3}). Porosity of the PVDF-TrFE conduits was calculated by SEM image analysis. Conduits were frozen in liquid nitrogen, cut into short sections with a scalpel, and attached to a glass microscope slides on a metal platform using carbon double-sided tape. Conduits were sputter coated with a layer of gold/palladium for 10 s (Desk V, DentonVacuum)
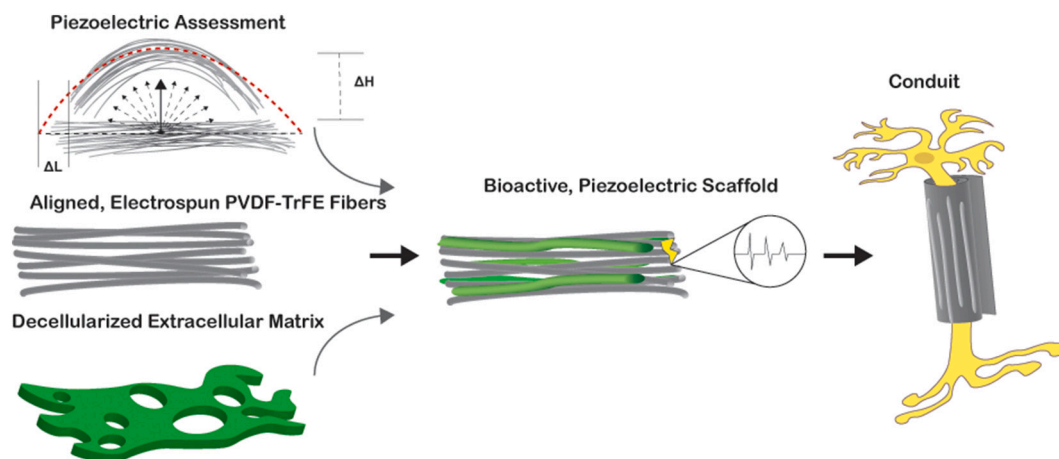
Fig. 1. Schematic detailing the multifaceted approach to the fabrication and assessment of PVDF-TrFE scaffolds for soft tissue repair. Aligned, piezoelectric fibers were assessed for electrical activity in response to applied mechanical deformation. Fibers were then incorporated with bioactive decellularized extracellular matrix. Finally, scaffolds were used to construct a novel conduit design that retains the physical, electrical, and biochemical properties that can augment the nerve regeneration process.

and imaged by SEM at an acceleration of 5 kV. SEM images with a low magnification were used to calculate conduit porosity, as previously demonstrated [19]. In brief, the proportion of pixels assigned to fiber area *versus* pore area was calculated using ImageJ software [20]. Thresholding was used to analyze grayscale levels of the SEM conduit image to create a binary image with pixels representing polymer fibers or pores within the conduit [19]. This method enhances the threshold through the maximization of the difference between threshold pixel values [21], thus creating two threshold values for either polymer fibers or pores.

Swelling of the PVDF-TrFE conduits was analyzed in Endotoxin-Free Dulbecco's PBS (1×) (w/o Ca++ & Mg++) (Millipore Sigma) for 24 h with n = 3 unique trials. Images of the conduit cross section in the upright position were taken before and after with a stereomicroscope (AmScope). Outer and inner diameter along with wall thickness were measured with ImageJ software. Hydrophobicity of PVDF-TrFE scaffolds was calculated using water contact angle with sessile drop technique on a First Ten Angstroms 1000 B Drop Shape Instrument. A drop of deionized water (5 μL) was deposited on the fiber mat surface and the left and right contact angles were measured and averaged.

Young's moduli of scaffolds were determined using 20 mm × 30 mm samples on a universal test machine (Test Resources Universal Test Machine). Samples were stretched at a rate of 1 mm min^{-1} parallel to the fiber alignment direction, and the resulting force and displacement recorded. Conduit samples were also prepared and analyzed using a universal test machine with n = 5 unique trials per condition. Trials were performed parallel to the alignment of the nanofibers. Conduits were stretched at a rate of 1 mm-min^{-1}. Force and displacement curves were converted to stress-strain curves where the slope of initial linear portion of curve was calculated.

Fourier transform infrared spectroscopy (FTIR) and X-ray diffraction (XRD) were used to evaluate the crystalline structure of the PVDF-TrFE scaffolds. Attenuated total resonance (ATR) FTIR (Nicolet 6700 FTIR with Smart Orbit diamond ATR) was used with a range of 4000–400 cm^{-1} and a resolution of 4 cm^{-1}. FTIR results provide a method of quantifying the relative fraction of β-phase, F(β), in the fibers by

$$F(\beta) = \frac{A_\beta}{(K_\beta/K_\alpha)A_\alpha + A_\beta} \tag{2}$$

where A_β and A_α are the absorbances at 840 cm^{-1} and 766 cm^{-1}, respectively. K_α and K_β represent the absorption coefficients at the respective wavenumber, which are 6.1×10^4 cm^2 mol^{-1} and 7.7×10^4 cm^2 mol^{-1}, respectively [22]. XRD (X'Pert Pro Diffractometer) was performed by irradiating the samples with monochromatic CuK$_\alpha$ with a scan rate of 0.013° s^{-1}. 2θ was kept between 15° and 43°.

2.3. Quantification of mechanical stimulation and piezoelectric output in PVDF-TrFE fibers

PVDF-TrFE scaffolds were subjected to cyclic mechanical stress to systemically evaluate piezoelectric response. The scaffold was deformed by lifting the middle of the scaffold while opposite ends were secured to a glass slide and covered with a layer of conductive silver paint for electrodes (Ted Pella Inc.). A 100 μm thick polydimethylsiloxane (PDMS) substrate was placed beneath fibers to facilitate deformation. Scaffolds were stretched both by hand and by a custom-built linear actuator powered by a motor (Polulu), with rotary encoding controlled by an Arduino Uno (Rev3) through the Arduino integrated development environment, with open-sourced code from the Arduino workshop (Supplemental Video S1) [23]. Hand stretching imparted greater forces on the scaffold to evaluate maximum possible current output, while the linear actuator provided a quantifiable, highly replicable, and programmable force. Long-term piezoelectric properties were evaluated by allowing the linear actuator to deform scaffolds for 10 min and comparing the electric response of the first 30 s to the final 30 s. Fibrous

scaffolds made of polycaprolactone (PCL), a non-piezoelectric polymer, were also examined.

PVDF-TrFE aligned, nanofiber conduits were also deformed using cyclic mechanical stress to evaluate piezoelectric capability. Conduits were compressed by "pinching" fibers with modified commercial tweezers attached to the actuator (Supplemental Video S2). The ends of the conduit were attached to a glass slide and coated with a layer of conductive silver paint for electrodes (Ted Pella Inc.). Conduits were compressed by hand to determine the maximum current produced and then compressed by linear actuation at a constant frequency to evaluate the current output over longer durations. During long-term compression testing with the linear actuator, conduits were compressed for 10 min, while the electric output was compared during the initial and final 30 s of the test. Aligned PCL nanofiber conduits were also analyzed. The estimated force applied by the actuator was recorded by a force sensing resistor (FSR® 402 Interlink Electronics) attached in series with the microcontroller circuit, where drops in voltage were calibrated with weights to determine the relationship between voltage and force.

2.4. Cell culture

NIH 3T3 fibroblasts (ATCC) and RT4-D6P2T Schwann cells (ATCC) were cultured in HyClone Dulbecco's high glucose modified eagle's medium (Cytiva) supplemented with 1 % Pen/Step and 10 % Bovine Calf Serum (BCS) or Fetal Bovine Serum (FBS), respectively. Cell cultures were incubated at 37 °C at 5 % CO$_2$ and 95 % relative humidity. Cells were grown for 72 h to subconfluence and routinely passaged using a phosphate buffered saline (PBS) (Thermo Fisher) wash and dissociation by 0.25 % trypsin (Gibco) in 1× Versene (Gibco).

PVDF-TrFE scaffolds were cut into oblong, 4 cm × 2 cm segments and attached to 18 mm × 1.5 mm circular coverslips and placed in a 12 well tissue culture plate (Falcon). Polytetraflouroethylene (PTFE) rings (Wilmad Labglass) were added to the scaffolds to ensure submersion after media incubation. Scaffolds were then pretreated for cell culture by exposure to UV-light followed by a 70 % ethanol rinse. Three subsequent PBS rinses were performed before incubating scaffolds in culture media overnight. For long-term cultures Schwann cells and fibroblasts were seeded at 50 cells mm^{-2} and examined at timepoints of 72 h, 1 week, and 2 weeks to assess viability. Cell media was changed every 3 days until day 10 when it was thereafter changed daily. For "In Situ hybrid" decellularized scaffolds, coverslips and scaffolds were incubated in a 0.2 % gelatin type A (Fisher) solution overnight.

2.5. Immunofluorescence microscopy

Rabbit polyclonal antibody to fibronectin (Abcam), rhodamine phalloidin (Invitrogen), and DAPI (4′,6′ – Deiamidino-2-Phenylindole Dihydrochloride) (Abcam) were used to immunolabel ECM (fibronectin), observe cell morphology (Phalloidin), and visualize cell nuclei (DAPI). Alexa Flour 488 Highly Cross-Absorbed Goat Anti-Rabbit secondary antibody (Thermo Fisher) was used for fluorescent detection of the primary fibronectin antibody.

Scaffolds were washed three times in PBS before fixation in 3.7 % formaldehyde for 15 min. Following two PBS washes, samples were permeabilized with 0.1 % Triton X-100 (Fisher) at 4 °C for 5 min and rinsed with PBS. Samples were incubated in a 1:100 dilution of primary antibody at 37 °C for 30 min followed by three PBS washes and a 1:100 dilution of rhodamine phalloidin (10 μg ml^{-1}) and Alexa Flour 488 secondary antibody (1 μg ml^{-1}) under the same conditions. Finally, scaffolds were incubated in 300 nM DAPI antibody and then mounted to glass microscope slides with antifade mounting medium (Abcam). Clear nail polish was used to seal coverslips.

Widefield microscopy images were captured using a Nikon Eclipse Ti2 inverted microscope with a Nikon DS-Qi2 camera. Confocal microscopy images were captured with a Nikon eclipse Ti inverted microscope on a Nikon AIR confocal. Confocal microscopy was used to assess three-

dimensional arrangement of cells within scaffolds, where a multi-channel Z-stack was performed at 1024-pixel resolution across the height of the scaffold. A representative maximum intensity projection and 3D projection using the DAPI, FITC, and TRITC channels were created. All analysis was performed using NIS Elements software.

Cell and ECM alignment was calculated using fluorescent images and NIH ImageJ software (version 1.52p), as previously described [11]. In brief, images were processed using a Fast Fourier Transformation (FFT), where resultant FFT spectra were detected using the oval profile plugin to quantify the pixel radial sums from 0 to 180 degrees. Full width, half maximum values were quantified for each curve where a lower FWHM indicated a larger, broader radial sums curve and thus greater alignment. Each experiment utilized 3 distinct coverslips with at least 15 images captured per coverslip.

2.6. Incorporation of dECM into PVDF-TrFE scaffolds

Functionalization of PVDF-TrFE scaffolds with a cell-derived ECM was developed and assessed in multiple configurations. This resulted in the formation of 3 bioactive "hybrid" scaffolds composed of PVDF-TrFE-dECM (Table 1).

In method 1, fibroblasts were seeded at a density of 50 cells·mm^{-2} and cultured in media supplemented with 50 μg·ml^{-1} of ascorbic acid (Fisher). After two days, media was freshly exchanged, and cells were cultured an additional five days, changing media again at day 3. Cells were then decellularized as previously described [12]. Briefly, incubation with a wash buffer (0.1 M Na$_2$HPO$_4$, pH 9.6, 2 mM MgCl$_2$, 2 mM EGTA) was performed, followed by incubation in lysis buffer (3 mM Na$_2$HPO$_4$, pH 9.6, 1 % NP-40) for 15 min at 37 °C, and further incubation in fresh lysis buffer for an hour. An additional wash buffer (0.3 M KCl, 10 mM Na$_2$HPO$_4$, pH 7.5) and 4× PBS rinses were performed before final storage in PBS. Scaffolds with dECM created using this method are referred to as "*in situ* hybrid" scaffolds (Table 1).

"*Incubated* hybrid" scaffolds were created using digested dECM that was then coated onto scaffolds. In short, dECM protein was derived using large, 15 cm culture dishes (Falcon) under the same conditions employed for decellularization of scaffolds. Following decellularization, accumulated dECM was mixed in a 1.5 mL centrifuge and stored in PBS. The resulting mixture was flash frozen with liquid nitrogen and lyophilized using a 2.5 L Freezone Freeze Dry System (Labconco). The lyophilized sample was frozen again with liquid nitrogen and milled, before being enzymatically digested with a 10:1 ECM:Pepsin ratio in 0.01 N HCl at room temperature over 48 h, as previously described [24]. Relative protein concentration of digested samples was determined by bicinchoninic acid assay (BCA) and typically fell between 1 and 4 μg ul^{-1} for every three 15 cm fibroblast culture plates.

A final hybrid scaffold, termed "*co-spun* hybrid," was fabricated by electrospinning the digested dECM-Pepsin solution directly with the PVDF-TrFE polymer precursor. For these scaffolds, 300 μl of 4.047 μg ul^{-1} digested dECM solution was added to the PVDF-TrFE polymer precursor solution and electrospun for 1 h.

Resulting bioactive hybrid scaffolds with dECM functionalization were all stored at 4 °C and summarized according to their fabrication parameters (Table 1).

2.7. dECM hybrid scaffold characterization

The three bioactive dECM-PVDF-TrFE hybrid scaffolds described in Section 2.6 were examined with SEM microscopy as described in Section 2.2. Both the *co-spun* and *in situ* hybrid scaffolds were visually distinct from normal PVDF-TrFE fibers and thus could be identified using electron microscopy. As the *incubated* hybrid scaffolds present with smaller proteins adhering to fibers, confocal microscopy was used to create a Z-stack image to visualize the fibronectin protein diffusion through the length of the scaffolds (Supplemental Fig. S1).

After verification of the incorporation of dECM to the PVDF-TrFE scaffolds with microscopy, FTIR and XRD were used to assess relative crystalline structure as described in Section 2.2. As *incubated* and *in situ* hybrid scaffolds only attach to surface of PVDF-TrFE, FTIR and XRD analysis was only performed on *co-spun* hybrid scaffolds.

2.8. Assessment of bioactive functionalization of PVDF-TrFE

The bioactive hybrid PVDF-TrFE scaffolds were examined for relative bioactive functionalization with gel electrophoresis, immunoblotting, and a cell viability assay. Whole cell lysates were prepared using NIH 3T3 fibroblasts at 50 cells·mm^{-2} on 6 well plates over 7 days, supplementing ascorbic acid at 50 μg mL^{-1}, and performing radio immunoprecipitation assay (RIPA, Abcam, ab156034) lysis with a 1× RIPA solution and a 7× Protease and Phosphatase Inhibitor Cocktail (Halt). Additional lysates were prepared using fibroblasts on PVDF-TrFE scaffolds and *co-spun* hybrid scaffolds. Finally, a *co-spun* hybrid scaffold was incubated in media for 7 days without cells and subjected to RIPA extraction and lysis as described.

Total protein levels of lysates were quantified with a BCA protein assay and analyzed with a 96-well microplate reader (Biorad). 10 μg of protein was extracted from each lysate and reduced with 1 M DTT (Thermo Fisher) and 2× Laemilli Buffer (Biorad). Lysates were boiled for 5 min at 96 °C and resolved on a 6–10 % SDS-acrylamide gel (Invitrogen). After electrophoresis, proteins were transferred onto a nitrocellulose membrane (106000004, GE Healthcare) using a Trans-Blot Turbo System (Biorad) and semi-dry transfer buffer. Membranes were blocked with a 3 % BSA in TBST (Tris-Buffered Saline, 0.1 % Tween-20) solution for 2 h.

Rabbit polyclonal anti-Fibronectin antibody (ab2413), Rabbit polyclonal anti-Laminin antibody (Abcam, ab11575), GDNF polyclonal antibody (Invitrogen), and Recombinant Anti-c-Jun antibody (Abcam, ab40766) were diluted at a 1:2000 ratio in blocking solution. Membranes were incubated in primary antibody solution at 4 °C overnight. Membranes were washed with TBST solution between incubations and subsequently incubated in either enhanced chemiluminescence (ECL) Rabbit IgG, HRP-linked secondary antibody (GE Healthcare) or enhanced chemiluminescence (ECL) Mouse IgG, HRP-linked secondary antibody (GE Healthcare) for 1 h at room temperature. Membranes were incubated in ECL Western Blotting Substrate (Pierce, Thermo Fisher) for an additional 5 min before imaging with the rapid-auto protocol on a ChemiDoc Imaging system (Biorad). Each blot was verified with two additional replicates. Anti-GAPDH monoclonal antibody (Invitrogen) was used as a loading control to verify equal protein loads across all sample lysates.

MilliporeSigma MTT, Calbiochem was purchased from Fisher Scientific and used to perform a colorimetric assessment of metabolic

Table 1
Summary of PVDF-TrFE scaffold configurations with bioactive modifications.

	PVDF-TrFE	In situ	Incubated	Co-spun
Fabrication	Electrospinning	Electrospinning	Electrospinning	Electrospinning
dECM Incorporation	N/A	7 days of fibroblast culture followed by decellularization *in situ*	Digested dECM incubated with PVDF-TrFE overnight	Digested dECM *co-spun* with polymer precursor solution

activity, as previously described [25]. NIH 3T3 fibroblast cells were used as a standard to create a linear absorbance curve for the colorimetric reduction of MTT by metabolic enzyme carriers, where the optical density detected by the microplate reader (Biorad) at 540 nm (OD_{540nm}) serves as an indirect measure of cell viability. Cells were seeded at 50 cells-mm^{-2} on either PVDF-TrFE scaffolds, or one of the three hybrid scaffolds described in Section 2.6: *co-spun, in-situ,* or *incubated.* An early timepoint of 4 h was used to examine initial adherence of cells to the scaffolds, while cells were examined for metabolic activity after 48 and 72 h. Briefly, at each time point the cultures were aspirated and replaced with fresh media supplemented with a 12 mM MTT solution. The contents of the 96-well plate were thoroughly mixed. Dimethyl sulfoxide (DMSO) was used to solubilize the reduced MTT (formazan) for 30 min before imaging relative absorbance.

2.9. Statistical analysis

Microsoft Excel and R Studio (version 4.02) were used to analyze fiber diameter, contact angle, Young's modulus, porosity, and other values. One-way analysis of variance (ANOVA) and Tukey's *post hoc* test were performed either with R Studio or Origin 9.1.

3. Results

3.1. Quantification of piezoelectric capacity in PVDF-TrFE scaffolds

PVDF-TrFE nanofiber scaffolds were fabricated by electrospinning with SEM images showing a strongly aligned and uniform morphology of the electrospun nanofibers and average fiber diameter of 791 ± 19.1 nm. Axial stress was applied to the PVDF-TrFE scaffolds either by hand or linear actuator (Fig. 2A, B), resulting in an alternating current output corresponding to the stretch and release of the scaffold (Fig. 2C). A positive current was observed during the stretch of the scaffold, and a negative current was observed when scaffold was released. PVDF-TrFE scaffolds were stretched by hand to impart a maximum force and strain on the fibers without breaking. A calibrated FSR was used to estimate the force imparted in the fibers (Supplemental Fig. S2A). With a force of approximately 0.2 N, a current of 20 nA was measured (Fig. 2C).
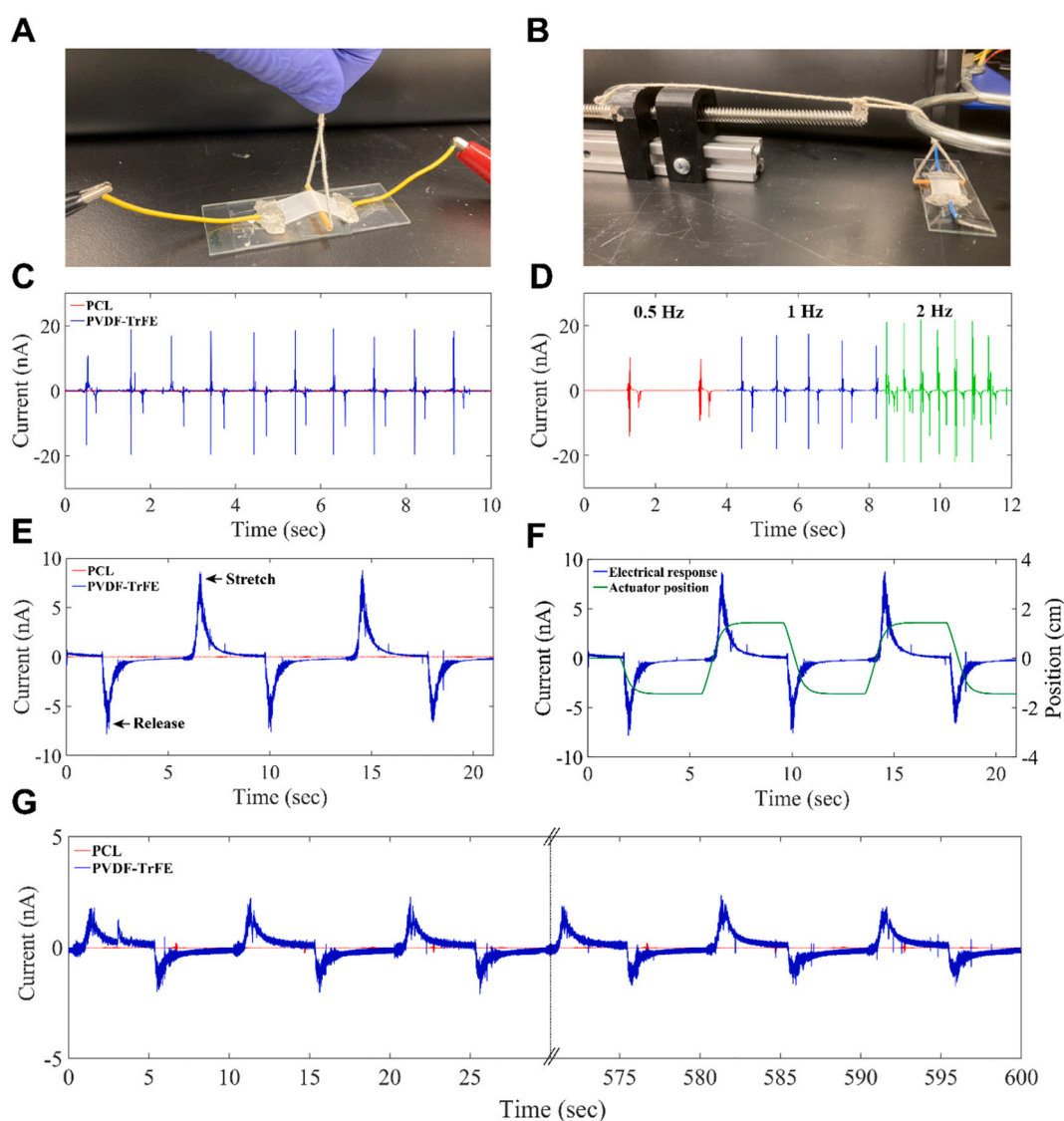
Fig. 2. Characterization of PVDF-TrFE scaffold piezoelectric output. (A) Experimental setup for piezoelectric output by hand stretching. (B) Experimental setup for piezoelectric output by linear actuator. (C) Comparison of measured current output of PVDF-TrFE and PCL scaffolds deformed by hand. (D) Current output of PVDF-TrFE scaffolds at 0.5 Hz, 1 Hz and 2 Hz frequencies. (E) Current output of PVDF-TrFE and PCL scaffolds deformed by cyclic stretching from automated linear actuator. (F) Linear actuator movement in centimeters (green) compared to electrical output of scaffolds in nanoamps (blue). (G) Current output of PVDF-TrFE and PCL scaffolds continuously stretched over a period of 10 min by linear actuator.

By comparison, non-piezoelectric polycaprolactone (PCL) scaffolds generated a maximum current of <1 nA (Fig. 2C). The frequency of stretching was also varied from 0.5 Hz to 2 Hz (Fig. 2D), with 0.5 Hz yielding the lowest current, of approximately 7 nA, compared to 18 nA at 1 Hz and a maximum current of 22 nA at 2 Hz. Increasing the frequency above 2 Hz did not produce a significantly larger current (data not shown). As the frequency of stretching increased from 0.5 to 2 Hz, a reduction in the output impedance occurs, leading to improved impedance matching with the measurement system and therefore higher electrical output [26].

PVDF-TrFE scaffolds were then deformed using a linear actuator to impart a consistent, quantifiable force and strain to the scaffold (Supplemental Video S1). Deforming the scaffold by 0.2 cm induced a positive current of approximately 8.5 nA (Fig. 2E). Conversely, releasing the fibers from the stretched position induced a negative current of approximately −8.1 nA (Fig. 2E). The position of the linear actuator was determined by a rotary encoder on the actuator motor and compared to the electrical output of the PVDF-TrFE fibers (Fig. 2F). The beginning of deformation corresponded with the beginning of the positive current peak, then as the linear actuator held the scaffold in the stretched position the current gradually returned to zero. Similarly, the start of the release of the scaffold aligned with the negative current peak, with the current returning to zero at the end of the release. The piezoelectric coefficient, d_{33}, of PVDF-TrFE nanofibers holds a large variance depending upon processing methods, with numbers ranging from 0.03 pC N^{-1} [27] to 25 pC N^{-1} [28]. Without poling, our PVDF-TrFE nanofibers would be expected to have a d_{33} value on the lower end of the range. The PVDF-TrFE nanofiber mats stretched by the linear actuator with a force of approximately 0.15 N would produce an estimated voltage 1.9 V, according to fundamental piezoelectric theory:

$$V = \frac{z * d_{33} * F}{\varepsilon_0 \varepsilon_r * A} \tag{3}$$

where V is the generated voltage, z is the length of the scaffold, F is the applied force, ε_0 is the permittivity in vacuum, ε_r is the relative permittivity of PVDF-TrFE and A is the cross-sectional area of the scaffold. Long term piezoelectricity of the PVDF-TrFE scaffold was evaluated by subjecting scaffold to continuous cyclical stretching of approximately 0.1 cm by the linear actuator over a period of 10 min, producing an output of approximately 2.2 nA (Fig. 2G). A comparison of the first and last 30 s of cyclical stretching reveals no degradation in electrical output over time.
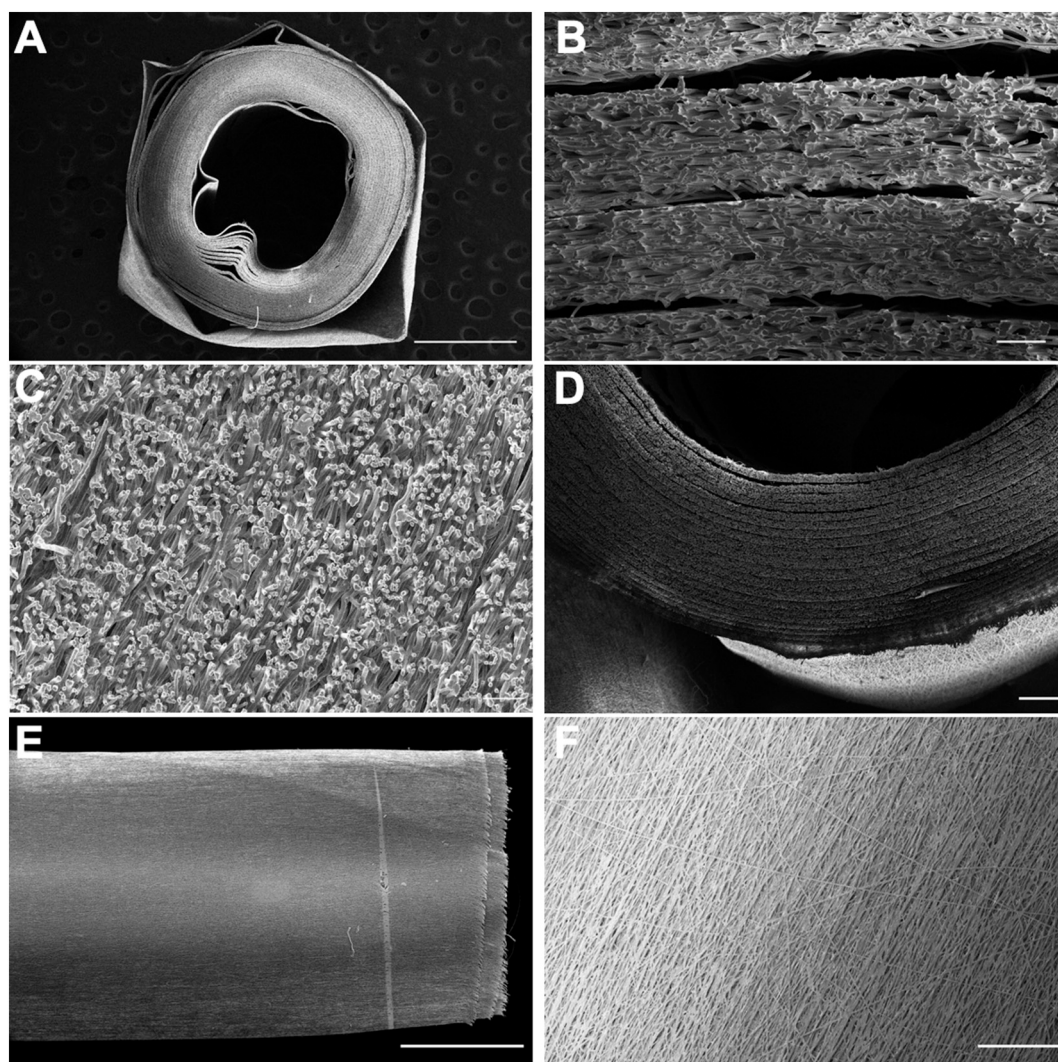
Fig. 3. SEM images of PVDF-TrFE conduits. SEM image of an electrospun PVDF-TrFE conduit cross-section at A) 25× magnification (scale bar = 1 mm), B) 1200× magnification (scale bar = 10 μm), and C) 1000× magnification (scale bar = 10 μm) showing nanofiber diameters. D) SEM image of an electrospun PVDF-TrFE conduit cross-section at 100× magnification showing wall thickness (scale bar = 100 μm). E) SEM image of an electrospun PVDF-TrFE conduit at 30× magnification (scale bar = 1 mm). F) SEM image of an electrospun PVDF-TrFE conduit at 200× magnification showing aligned nanofibers (scale bar = 100 μm).

3.2. Characterization and piezoelectricity of PVDF-TrFE conduits

Piezoelectric PVDF-TrFE electrospun scaffolds were then used as the platform to build 3D nerve guidance conduits for translation. Aligned, electrospun scaffolds were fabricated and rolled into a tube to produce the conduits. Conduits were 19.87 to 22.35 mm long with an outer diameter between 2.47 and 2.73 mm (Fig. 3A). Individual conduit length is highly tunable and can be modified depending on injury gap lengths. Conduits possessed an individual layer thickness of approximately 22 μm and a wall thickness between 0.38 and 0.51 mm (Fig. 3B, D). A conduit wall thickness of 200 μm was determined to be the lower limit for overall thickness while still allowing for adequate nutrient diffusion [29], while a wall thickness of 600 μm was determined as the upper limit for conduit thickness [30].

Conduits retained fiber alignment present in scaffolds, with alignment oriented lengthwise down the conduit to provide physical guidance for cell migration (Fig. 3E, F). Conduit fibers had an average fiber diameter of 791 ± 19.1 nm and exhibited an average porosity of 52.5 ± 1.2 % (Table 2), with interconnected pores (Fig. 3B, C). Swelling of the conduits resulted in an increased wall thickness of approximately 2.19 %. Mechanical testing of the elastic moduli for the nerve guidance conduits was performed in the direction of the longitudinally aligned fibers with a mean elastic modulus of 57.91 ± 6.12 MPa (Table 2).

Piezoelectric output of conduits was analyzed by measuring the electric current produced due to mechanical compression of the conduit (Fig. 4A, B, Supplemental Video S2). Compression was applied by pinching the middle of the conduit with tweezers, both by hand and actuator, which produced an alternating current (Fig. 4C, D). Compression by hand was performed to determine the maximum output current (Fig. 4C). A calibrated FSR was used to calculate the force exerted on the fibers (Supplemental Fig. S2B). A maximum current of 2.85 nA was measured when compressed by a force of approximately 0.58 N. As a control, PCL conduits produced a maximum current <0.3 nA. PVDF-TrFE conduits were compressed by linear actuator with a force of approximately 0.14 N producing a positive current of a 2.30 nA, while the PCL conduits produced a current <0.3 nA. Compression of conduits was also mapped to linear actuator position, showing that movement of the conduits resulted in piezoelectric output (Fig. 4D). The conduits were then compressed by linear actuator over a period of 10 min where a force of 0.14 N produced a positive current of approximately 2 nA, while PCL conduits produced a current <0.3 nA (Fig. 4E).

3.3. PVDF-TrFE scaffolds promote adhesion and proliferation in Schwann cells and fibroblasts

To assess the ability of electrospun scaffolds to allow cell adhesion and proliferation of both Schwann cells and fibroblasts, cells were grown on PVDF-TrFE scaffolds and analyzed. Both Schwann cells and fibroblasts adhered to scaffolds and elongated in the direction of the aligned fibers. Further, cell viability was maintained for a minimum of 14 days of culture (Fig. 5A). Importantly, both Schwann cells and fibroblasts integrated into the 3D scaffold and assembled a robust extracellular

matrix (Fig. 5Bi). It was also observed that the resultant three-dimensional culture of cells was highly aligned in the direction of the fibers (Fig. 5B). Thus, for extended culture periods, PVDF-TrFE scaffolds are an ideal biocompatible scaffold for creating a robust model for soft tissue repair.

3.4. PVDF-TrFE Scaffolds induce the formation of an aligned, bioactive extracellular matrix

Electrospun, aligned PVDF-TrFE scaffolds promote aligned cellular phenotypes as seen in our previous work [8], however the deposition of the underlying extracellular matrix was not previously investigated in depth. As the scaffold is 3D with cells permeated throughout, ECM will be deposited throughout scaffold depth (Fig 5Bii). Therefore, cell-secreted ECM assembly was assessed by observing fibronectin fibril formation, a ubiquitous ECM protein key to matrix assembly [31,32]. PVDF-TrFE scaffolds aligned both Schwann cells and fibroblasts parallel to the fiber orientation (Fig. 5C). Cells were able to migrate throughout the entire depth of the scaffold and confluent cells were observed at all depths of scaffold when imaged by confocal microscopy. Fibroblasts were grown on both unaligned and aligned scaffolds for 7 days and then decellularized [11]. PVDF-TrFE scaffolds were capable of secreting and assembling a robust ECM that could be successfully decellularized to derive an aligned decellularized extracellular matrix in the scaffold (Fig. 5C).

Scaffolds were analyzed for DAPI to ensure the absence of DNA following the decellularization procedure. SEM imaging further confirmed the absence of cells or cellular debris, while visualizing the complex, aligned matrix interspersed throughout the scaffold (Fig. 5D). Additionally, to determine the extent to which the PVDF-TrFE scaffolds can induce alignment of ECM, and retain alignment after decellularization, fibronectin fibril alignment was quantified before and after decellularization wash procedures on both PVDF-TrFE scaffolds and glass coverslips. ECM fibrils were significantly more aligned on aligned PVDF-TrFE scaffolds both before and following decellularization (Fig. 5E).
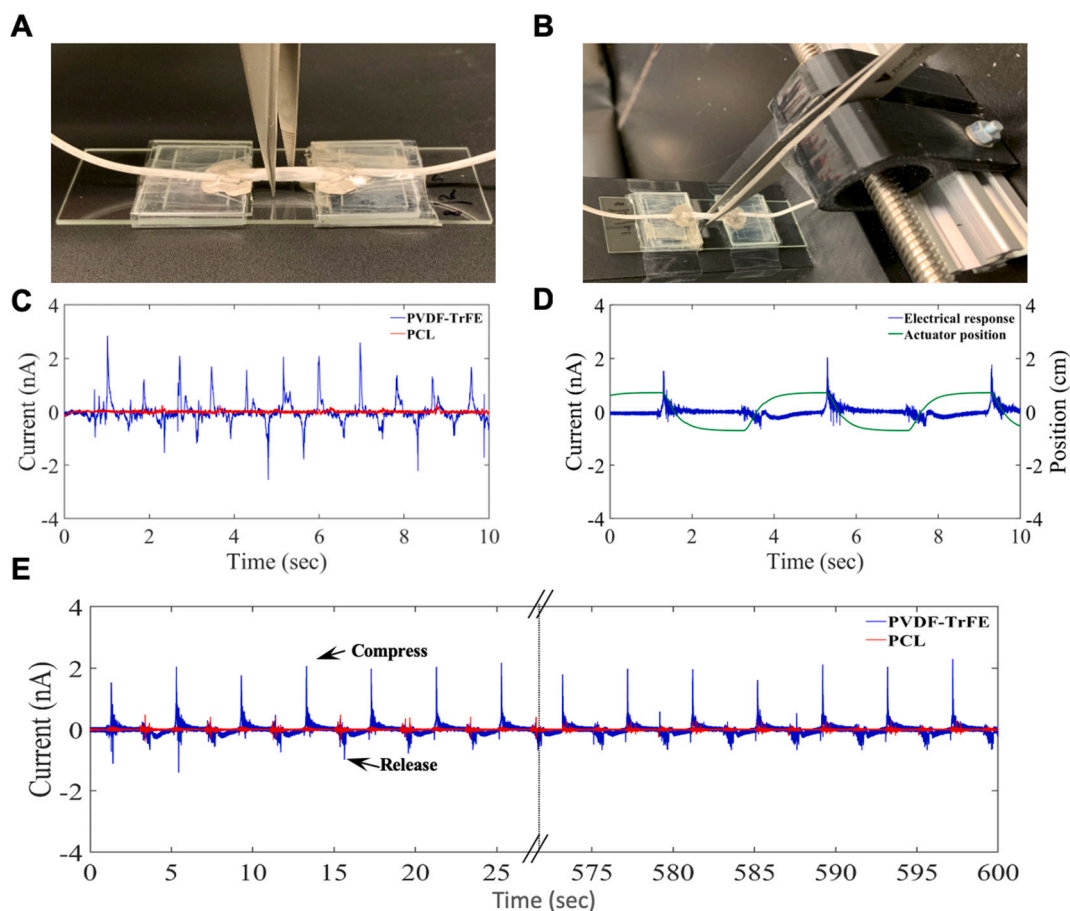
3.5. Direct functionalization of PVDF-TrFE scaffolds utilizing decellularized ECM

The ability to functionalize new materials to integrate with cells and tissue using proteins and other macromolecules is crucial to the future development of biomaterials for regenerative medicine. dECM represents a highly promising method for incorporation of a tissue specific, native bioactivity to scaffolds. Therefore, three distinct methods for fabricating aligned, electrospun fibers decorated with fibroblast-derived ECM were examined. In combination, these methods provide enhanced bioactivity and tissue integration to the piezoelectric scaffolds and conduits that have been developed and quantified for electric potential.

The first method, termed "*in situ* hybrid" method, was as described in the previous section where fibroblast cells were grown on PVDF-TrFE scaffolds (Fig. 5A, B) for 7 days and decellularized (Fig. 5C). After 7 days, three dimensional ECM was formed within scaffolds and was visualized by immunofluorescence and SEM (Fig. 5C, D).

PVDF-TrFE scaffolds were also functionalized by an "*incubated* hybrid method," where dECM solution was coated overnight on piezoelectric nanofiber scaffold. The fibronectin component of the dECM was detected in a three-dimensional array interspersed throughout the entire volume of the scaffolds (Supplemental Fig. S1).

Finally, a comprehensive "*co-spun* hybrid" method was developed for incorporation of dECM directly into PVDF-TrFE fibers, without the need to preculture cells or incubate proteins on scaffolds or conduits. An enzymatic digestion of lyophilized, cell-assembled dECM was performed to provide a solubilized solution of dECM proteins as was used in the *incubated* hybrid method. The solution was then electrospun to produce fibers with dECM directly embedded throughout the scaffold (Fig. 6A).

Table 2
Summary of fiber diameter, porosity, Young's modulus, water contact angle and relative fraction of β-phase of PVDF-TrFE scaffolds and PVDF-TrFE/ECM hybrid scaffolds and PVDF-TrFE nerve guidance conduit.

PVDF-TrFE Scaffold	Fiber diameter (nm)	Porosity (%)	Young's modulus (MPa)	Contact angle (°)	F (β) (%)
No ECM	791 ± 19.1	74.1 ± 2.32	4.01 ± 1.57	129 ± 1.24	72.1
Co-spun ECM	428 ± 10.1	84.9 ± 1.13	2.89 ± 0.89	121 ± 0.87	74.3
Conduit	791 ± 19.1	52.5 ± 1.2	57.91 ± 6.12	N/A	72.1

Fig. 4. Piezoelectric characterization of PVDF-TrFE conduits. (A) Experimental setup for the measurement of piezoelectric output by hand compression. (B) Experimental setup for the measurement of piezoelectric output by linear actuator compression. (C) Measured current output of aligned PVDF-TrFE and PCL conduits by hand compression at a frequency of 1 Hz. (D) Plot of position *versus* time of linear actuator during compression testing of PVDF-TrFE conduits. Positive peak on the positional plot correlates to the full compression of the conduit and the negative peak correlates to the full release of the conduit. (E) Measured current output of aligned PVDF-TrFE and PCL conduits by linear actuator compression for a duration of 10 min.

The *co-spun* hybrid dECM-hybrid scaffolds showed a uniform morphology with aligned fibers. Interestingly, the fiber diameter of the dECM-hybrid scaffolds was smaller compared to plain PVDF-TrFE scaffolds (Table 2), which can potentially be attributed to differing solvent composition with dECM. Further, the *co-spun* hybrid scaffolds had a porosity of 84.9 %, making them more porous than plain PVDF-TrFE scaffolds with a 74.1 % porosity. *Co-spun* hybrid scaffolds also had a lower mean Young's modulus value (2.89 ± 0.89 MPa) than the plain PVDF-TrFE scaffolds (4.01 ± 1.57 MPa) (Table 2). Cells were grown on *co-spun* hybrid scaffolds and shown to facilitate robust attachment and growth (Fig. 6B).

3.6. Functionalization of PVDF-TrFE with bioactive dECM promotes a regenerative microenvironment

Both plain and bioactive PVDF-TrFE scaffolds were then used to examine the expression of key regenerative proteins upregulated in the PNS repair process. Western blot analysis showed that PVDF-TrFE scaffolds, with or without functionalization, promoted greater expression of fibronectin and laminin-1 protein, two key components of soft tissue extracellular matrix when compared to polystyrene culture dishes (Fig. 6C). Bioactive functionalization through the *co-spun* hybrid method without cells (from left to right lane 4) and with the addition of cells (lane 5) both induced greater expression of the matrix proteins fibronectin and laminin-1, and comparable expression of regenerative neurotrophic factors c-jun and GDNF (Fig. 6C). Notably, the presence of

PVDF-TrFE, with or without dECM functionalize, also induced secretion and deposition of extracellular matrix, as described previously in Section 3.4. c-Jun and GDNF were also analyzed as key markers in PNS repair [1,33], with both *co-spun* hybrid scaffolds and plain PVDF-TrFE scaffolds showing a drastic increase in expression compared to polystyrene (Fig. 6C). While protein expression in unmodified whole cell lysates (lane 1) was relatively sparse, NIH 3T3 fibroblasts are commonly used to detect expression of various proteins through immunoblotting and it can be inferred that PVDF-TrFE scaffolds were the primary driver of matrix protein expression and the presence of regenerative neurotrophic factors.

3.7. Co-spun hybrid scaffolds retain piezoelectric capacity

To ensure that the incorporation of dECM did not hinder the piezoelectric capacity of the scaffolds, Fourier transform infrared spectroscopy (FTIR) and X-ray diffraction (XRD) analysis were performed on *co-spun* hybrid scaffolds. Comparison of the resulting spectra for the bioactive, integrated *co-spun* hybrid scaffold and unmodified PVDF-TrFE scaffold resulted in no significant differences (Fig. 6D). Both spectra showed characteristic peaks of the β-phase of PVDF-TrFE at 470, 840, 880, 1275 and 1399 cm^{-1} wavelengths [9,22,34]. Further, a small shoulder at 1117 cm^{-1} was present in both samples (Fig. 6D), indicative of the λ-phase [35]. The XRD pattern of the PVDF-TrFE scaffold showed a strong diffraction peak at $2\theta = 19.8°$, corresponding to the 110/200 reflection of the orthorhombic β-phase crystal [34,36]. The *co-spun*
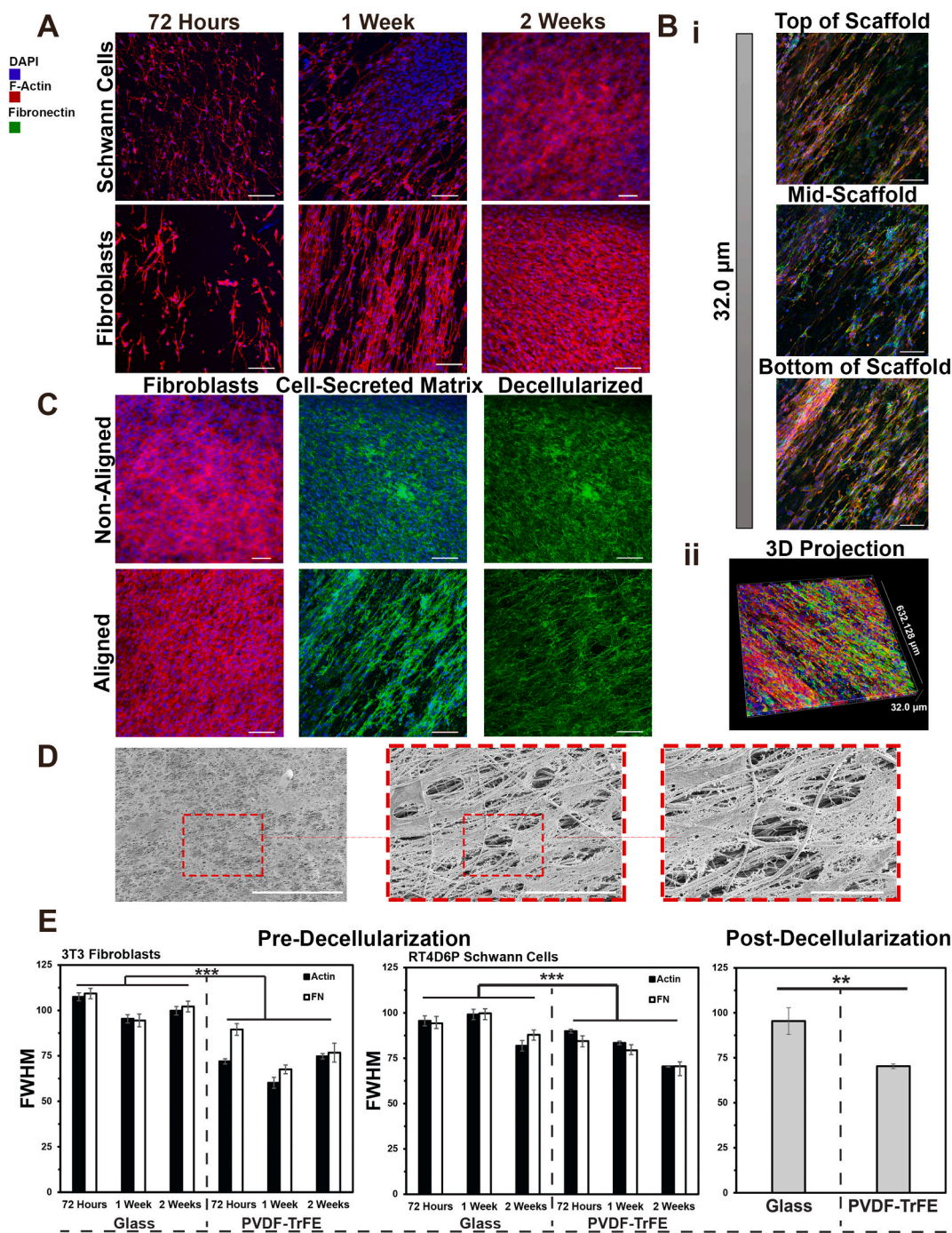
Fig. 5. Schwann cells and fibroblasts integrate with PVDF-TrFE scaffolds to secrete and assemble a robust, extracellular matrix. (A) Schwann cells and fibroblasts adhere, align, and remain viable on PVDF-TrFE scaffolds for 72 h, 1 week, and 2-week time points. Scale bars = 100 μm unless otherwise noted. (B) Aligned PVDF-TrFE scaffolds induced alignment of cells and the formation of an aligned, cell-assembled fibronectin matrix. (i) Scaffolds allowed for the diffusion of cells and proteins throughout the entire depth of the scaffolds (ii) 3D projection of cells and fibronectin ECM on scaffolds further ensures the presence of an organized, aligned matrix throughout the height of the scaffold. (C) Aligned PVDF-TrFE scaffolds induced the secretion and formation of an aligned ECM that was decellularized to produce an aligned dECM biomaterial. (D) SEM microscopy confirms the presence of an aligned, decellularized ECM interspersed throughout the PVDF-TrFE fibers. Scale bars = 500, 50, and 20 μm, respectively. (E) Full Width Half Maximum (FWHM) values show alignment of both cells and fibronectin matrix Pre-Decellularization as well as dECM alignment Post-Decellularization in comparison to glass coverslips. Data are reported as mean ± SEM. *$p \le 0.05$; **$p \le 0.001$; ***$p \le 0.0001$.

hybrid scaffolds likewise presented a peak at $2\theta = 19.8°$. To provide a more quantitative comparison of the scaffolds with and without ECM, the relative fraction of β-phase was estimated using Eq. (2). PVDF-TrFE scaffolds had a 72.1 % fraction of β-phase as compared to 74.3 % from the *co-spun* hybrid scaffolds, showing no decrease in the piezoelectric β-phase after functionalization with dECM.

3.8. Incorporation of bioactive dECM in scaffolds promotes the metabolic activity of Schwann cells and fibroblasts

NIH 3T3 fibroblasts were grown on all three bioactive (Table 1; *in situ*, *incubated*, and *co-spun*) variations of the PVDF-TrFE scaffolds and analyzed for metabolic activity at three distinct time points. The
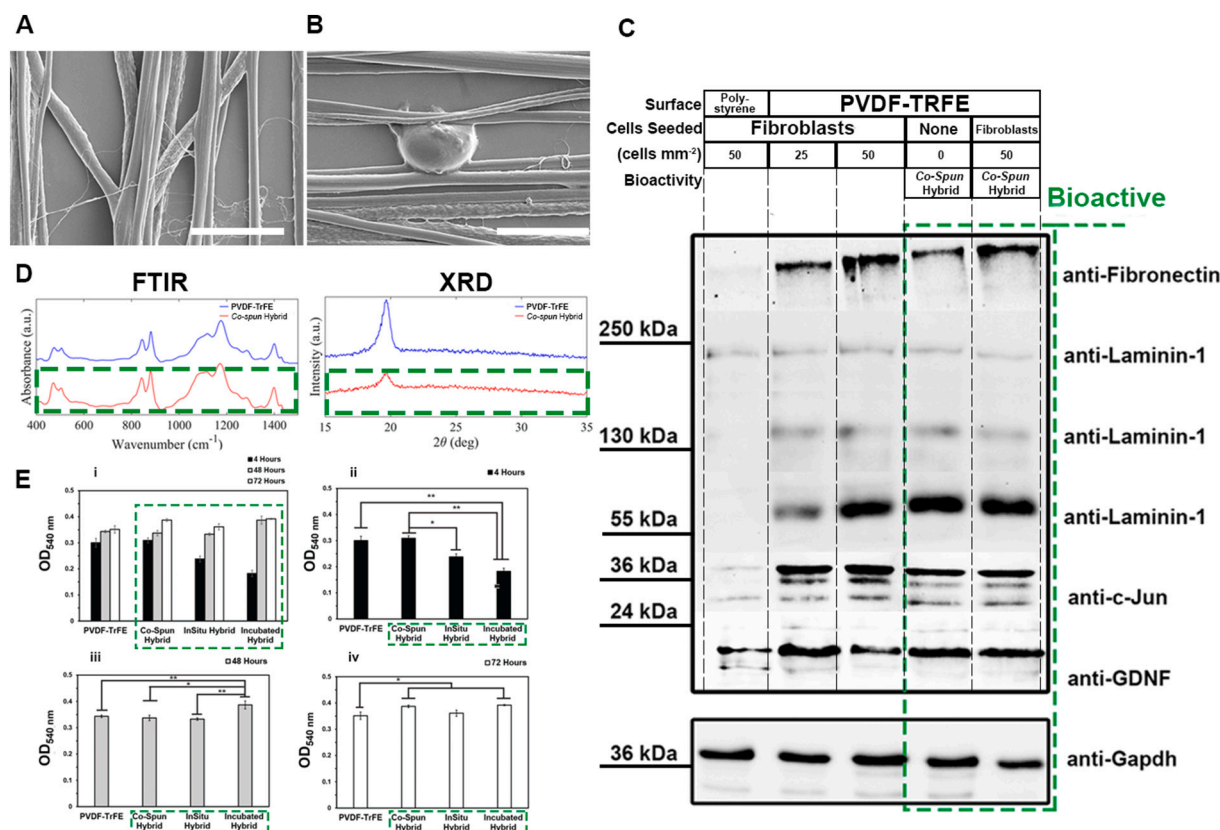
Fig. 6. dECM was successfully integrated into PVDF-TrFE scaffolds through multiple approaches. (A) A "*co-spun* Hybrid" PVDF-TrFE scaffold demonstrating integration with dECM. Scale bar = 20 μm. (B) NIH 3T3 fibroblast cell on the *co-spun* Hybrid scaffold. Scale bar = 20 μm. (C) Fibroblasts cultured on tissue culture polystyrene dishes (lane 1 from left to right), on PVDF-TrFE scaffolds (lane 2 and 3), *co-spun* hybrid PVDF-TrFE scaffold without fibroblasts (lane 4), and *co-spun* hybrid scaffolds with fibroblasts (lane 5), exhibit significant differences in the expression of key matrix proteins and key PNS regenerative factors. (D) FTIR and XRD spectra show no reduction in β-phase configuration upon incorporation of dECM in the *co-spun* hybrid scaffolds. (E) Despite differences in initial cell adhesion after 4 h (i) both the *co-spun* hybrid and *incubated* hybrid dECM scaffolds promoted elevated levels of cell viability (ii), 48 (ii), and 72 h (iv) of culture. Data are reported as mean ± SEM. *$p \leq 0.05$; **$p \leq 0.001$; ***$p \leq 0.0001$.

colorimetric MTT-Viability assay was used to create a standard absorbance curve for living cells in which the corresponding metabolic activity could be measured by optical density of a standard microplate reader at 540 nm (Supplemental Fig. S3). Early cell adhesion was variable depending on incorporation method of dECM. *In situ* hybrid scaffolds and *incubated* hybrid scaffolds exhibited relatively low initial cell adherence after 4 h (Fig. 6Ei, ii). However, after 48 h the *incubated* hybrid scaffolds induced greater activity of fibroblast cells than standard PVDF-TrFE (Fig. 6Eiii). Finally, after 72 h both the *incubated* hybrid and *co-spun* hybrid scaffolds exhibited greater fibroblast viability, while *in situ* hybrids were comparable to PVDF-TrFE scaffolds (Fig. 6Eiv). Thus, after multiple days of culture it was determined that dECM can be successfully incorporated into PVDF-TrFE scaffolds to impart a positive proliferative impact on fibroblast cells. This work paves the way for potential use of the PVDF-TrFE nanofiber scaffolds in PNS tissue repair while providing multiple novel methods of bioactive functionalization with a robust biomaterial.

4. Discussion

Here we have developed a highly tunable, electrospun biomaterial fabricated to possess the physiologically relevant mechanical, electrical, and biochemical signaling necessary for wound repair, specifically in traumatic PNS injury. The piezoelectric PVDF-TrFE biomaterial was engineered to incorporate bioactive, cell-assembled dECM through multiple mechanisms, and the resulting bioactive biomaterial can be utilized as a non-invasive electric stimulant to tissue and cells. The highly porous nature of the electrospun PVDF-TrFE scaffold is also vital

to provide the needed mechanical properties of the scaffold, enhanced cell adhesion and proliferation, and necessary requirements for fabrication of a conduit for prospective nerve applications.

Piezoelectricity has been utilized in non-tissue engineering applications previously and holds significant physiological relevance, as the phenomenon is observed in collagen, DNA, and living tissue [7,37,38]. However, there is currently a limited knowledge underlying the ability of piezoelectric biomaterials to transmit cell or tissue level deformations into the appropriate electric signals needed or desired for regeneration. In non-tissue engineering work many groups have analyzed macro-level deformations of piezoelectric material, as the energy harvesting potential is large. In biomedical work, Nunes-Pereira et al. showed that small taps by a human finger can generate a voltage of 5.02 V and power up to 25 μW from PVDF-TrFE electrospun scaffolds with barium titanate (BaTiO$_3$) nanoparticles, enough to power many small biosensing and biomedical devices [39]. However, despite a conclusion that this output is not influenced by cyclic frequencies, our work showed the ability to achieve different current amplitudes across multiple cyclic intervals while producing replicable currents.

Recently, it has been shown that applying currents in the nanoamp range to aqueous solutions can modulate signal transduction pathways involved in inflammatory responses of mesenchymal stem cells, which can enhance peripheral nerve regeneration by altering the inflammatory environment in surrounding tissue [40,41]. We show emphatically that the indirect movement of actuation, as recorded by real-time motor encoder counts across deformations of 0.2 cm, corresponds to a resultant current amplitude of approximately 9 nA. Other groups that have applied similar cyclical bending stimuli to PVDF-TrFE nanofiber mats

have reported an electrical response of approximately 1 V and 15 nA [42]. Based on other piezoelectric models of electrospun PVDF-TrFE as a sensor, of similar fabrication and thickness, our maximum current of 22 nA corresponds to an approximate maximum voltage of 1.5 V [42]. Similarly, based on the piezoelectric theory using an estimated piezoelectric coefficient, we can approximate the upper range of voltage being produced to be around 1.9 V. Researchers have shown stimulated piezoelectric material outputting voltages of 0.07 to 0.19 mV enhanced neurite growth, cell differentiation, and maturation *in vitro* and electric stimulation in the range of 0.02 to 10 V has resulted in quicker functional recovery of facial nerves in humans [43]. Additionally, other groups have attempted to characterize the piezoelectric potential through different means. For instance, Gryshkov et al. examined the effect of variable concentration loads of PVDF-TrFE by examining zeta potential after electrospinning and correlating results to the piezoelectric strain constant [44]. However, a more refined model correlating the electric response to different stimulation methods may prove beneficial to the further understanding and application of piezoelectric biomaterials.

Schwann cells, a key cell type in PNS regeneration, interact with the ECM and surroundings through mechanical and electrical signaling, and undergo phenotypic changes following injury. For instance, in addition to a complex upregulation of markers such as c-Jun, and MAPK signaling [13], Schwann cell response to initial nerve transection is characterized by an immediate promotion of cytoplasmic calcium, which initially catalyzes the breakdown and clearance of myelin debris post-injury, while also potentially remodeling the Schwann cell cytoskeleton [45]. Additionally, neuronal production of calcium is a key neurotransmitter that, in downstream post-healing stages, is a measure of both Schwann cell-axon cross-communication [46], the reinnervation of electrophysiological muscle, and non-nervous system tissue as well [47]. Applied electrical stimulation simulating an action potential can be used to promote regenerative markers in fibroblasts, such as proliferation and the increased secretion of collagen and other ECM components thought to be vital to successful nerve repair, though debate remains over the direct excitability of fibroblasts and the corresponding role of the ECM in transmitting such signals, and in turn enhancing favorable fibroblast gene expression such as transforming growth factor beta (TGF-β) [48]. Furthermore, electric stimulation has been shown to enhance production of regenerative factors, by upregulating cAMP signaling in DRGs and thus inducing axonal regeneration through increased neurotrophic factors and cytoskeletal proteins as well as an increase in calcium dependent production of nerve growth factor in Schwann cells *in vitro* and *in vivo* [49,50]. Ultimately, the synergistic effect between PNS cells and the surrounding microenvironment is, itself, a cross sectional understanding of electromechanical interaction. Thus, conductive biomaterials have demonstrated significant efficacy for neural repair applications, and electrospun scaffolds present an optimal platform for facilitating conductivity [51–55].

To begin to address PNS regeneration using electrospun PVDF-TrFE, scaffolds were used to develop hollow nerve guidance conduits (NGC). NGCs possess the ability to guide regeneration across the injury space and allow for the accumulation of glial cells, ECM, and growth factors while minimizing invasion of surrounding tissue [56]. The design of NGCs can be incredibly varied and tunable, but it is vital that conduits possess proper mechanics to support tissue level forces and hold any necessary surgical sutures in place. Hollow nerve conduits may not produce complete nerve regeneration over long injury lesions and are thus typically recommended for injury gap sizes of <3 cm in sensory nerves [57]. *In vivo* studies have evaluated the effectiveness of hollow nerve guidance conduits for peripheral nerve injury gaps of various lengths, and some have demonstrated positive results [58]. Xu et al. fabricated a hollow PDLLA/Chondroitin sulfate/Chitosan NGC and found that after 3-and-6-month intervals, the regenerated nerve, myelin fiber density, and myelin thickness were less than the autologous nerve graft control. However, adding nerve growth factor (NGF) to the conduit

significantly increased nerve regeneration and exhibited comparable regeneration to the nerve autograft [50].

Our work establishes that the piezoelectric potential of PVDF-TrFE scaffolds is maintained when fabricated into a conduit for future *in vivo* applications. In general, the piezoelectric capacity of conduits will be stimulated by macroscale bodily movements such as treadmill walks, interstitial fluid, and cell-traction forces [59] which may help to promote wound healing. Here we present a design for a robust, cylindrical conduit that maintains precise fiber alignment, ample porosity for the diffusion of key nutrients, and sufficient isolation from non-endoneuria cell infiltration [60]. Mechanical considerations for the development of conduits are extensive. The high porosity of electrospun scaffolds helps to aid in cell migration and cell growth, while preventing over-accumulation and potential Schwannoma or tumor like behavior [61]. This presents an inherent dichotomy, as porosity (and pore size) are increased the mechanical integrity of the conduit will be reduced [62]. Therefore, NGCs should possess a porosity >50 % to allow for nutrient and waste exchange [19,63], yet a porosity >80 % usually results in mechanically unstable conduits [19,63]. In comparison, our conduit porosity of 52.5 ± 1.2 % is within the desired range to allow nutrient and waste exchange while maintaining structural integrity.

The stiffness, or Young's Modulus, of electrospun fibers also has a significant effect on determining the fate of multipotent cell phenotypes [13,14,64,65]. PVDF-TrFE conduits possessed a modulus of 57.91 ± 6.12 MPa, which is greater than the 13.79 ± 5.48 MPa observed in native sciatic nerve tissue of rats [66] and the 40.96 ± 2.59 MPa seen in human sciatic nerve [67]. Similar work has shown that PVDF-PCL conduit hybrids manufactured through a casting and annealing process yielded an elastic modulus of 67.76 ± 2.64 MPa [68]. Additionally, it has been shown that the water content of a conduit is inversely related with its mechanical strength. However, when subjected to long-term swelling experiments, PVDF-TrFE conduit wall thickness increased by 2.19 %. These values all show our work to begin within acceptable ranges for translatable therapies moving forward.

While biomaterials are commonly functionalized with small peptides to induce a regenerative or desired cellular effect, dECM can be derived as an entirely independent protein matrix that demonstrates immense potential in PNS repair. However, care must be taken to retain many of the key regenerative functions of dECM in biomaterial design. Additionally, there has only been limited work demonstrating the incorporation of dECM for neural engineering purposes [52,69–73], and successful integration of 3T3-derived matrix to PVDF-TrFE fibers is unexplored. Multiple successful methods were used in this work to incorporate and analyze cell-secreted dECM into PVDF-TrFE scaffolds: 1) An "*in situ* hybrid" method of growing cells on scaffolds followed by decellularization and retaining bioactivity, 2) an "*incubated* hybrid" method where ECM was digested and coated onto scaffolds, and 3) a "*co-spun* hybrid" method where dECM was digested and electrospun in conjunction with PVDF-TrFE, directly embedding the proteins and factors in the biomaterial. Native ECM is highly organized, and alignment is especially crucial in nerve repair to direct axons and cells to their distal targets. Excitingly, using PVDF-TrFE fibers makes it possible to precisely align cells and to secrete, assemble, and remodel an ECM while promoting the expression of key signaling markers for regeneration in Schwann cells and fibroblasts such as c-Jun and GDNF through morphological alignment, as has been previously shown [13,14]. As ECM is assembled on the scaffold, the alignment of both cells and the cell-secreted ECM is maintained to create an ample regenerative environment. This effect is natively observed in mammalian neural tissue to drive axonal regeneration, when Schwann cells transdifferentiate to elongate and form aligned ECM bridges that provide physical and trophic support to the damaged tissue [1,15,74].

The secretion and assembly of an aligned, 3D ECM by cells demonstrated the ability of PVDF-TrFE scaffolds to induce a favorable response for nerve regeneration. Scaffolds were able to induce cells to secrete and assemble ECM, and then be successfully decellularized, leaving behind

physiologically relevant proteins and neurotrophic factors. Traditional methods of adding bioactive functionalization to biomaterials, such as decoration with peptides, fails to recapitulate the complexity of the ECM and its constituents *in vivo*. One of the fundamental advantages of electrospun fibrous scaffolds is their ability to be constructed in a biomimetic physical structuring that emulates the native ECM. The integration of dECM directly into the PVDF-TrFE precursor solution (*co-spun* hybrid) comprises the most replicable, translational approach for downstream *in vivo* applications as it mimics the complexity of the native ECM structure while depositing key regenerative factors throughout that can lead to functional recoveries.

5. Conclusion

This work comprises a systematic exploration of electrospun PVDF-TrFE scaffolds *in vitro* that demonstrates multiple unique advantages over traditional PNS-based biomaterials with unique chemical, physical, and electric signaling capabilities. The approach to creating and quantifying the electrospun, piezoelectric capacity of PVDF-TrFE scaffolds, both as fibrous scaffolds and fibrous conduits, provides new insight into the relationship between large, macro-level mechanical forces and the corresponding electrical potential that can be used for tissue and cell stimulation. Novel characterizations of scaffold piezoelectricity affirm the potential of piezoelectric materials as energy harvesters. These advantages are retained when scaffolds are used to fabricate hollow nerve guidance conduits that can be used for downstream applications. Finally, three methods were demonstrated to functionalize scaffolds and conduits with bioactive, cell-derived dECM. These methods were each capable of promoting greater viability of cells while inducing the expression of regenerative matrix proteins like fibronectin and laminin. Additional assessments ensured the robust incorporation of dECM and that it did not hinder the native piezoelectric capacity of PVDF-TrFE. Taken together, this work provides the framework to further develop bioactive, PVDF-TrFE biomaterials as alternative therapeutic devices that can be noninvasively activated to repair severe nerve damage.

Supplementary data to this article can be found online at https://doi.org/10.1016/j.bioadv.2022.213081.

Data availability

The raw data were generated at the University of Cincinnati. Derived data supporting the findings of this study are available from the corresponding author upon reasonable request.

CRediT authorship contribution statement

Conception and design of study: GM Harris; JA Orkwis; L Esfandiari; AK Wolf; ZJ Mularczyk.

Acquisition of data: JA Orkwis; AK Wolf; ZJ Mularczy; AE Bryan; CS Smith; R Brown; M Krutko.

Analysis and/or interpretation of data: JA Orkwis; AK Wolf; ZJ Mularczyk; CS Smith; AE Bryan; A McCann; RM Collar; L Esfandiari; GM Harris.

Drafting the manuscript: JA Orkwis; AK Wolf; ZJ Mularczyk; A Bryan; L Esfandiari; GM Harris.

Revising the manuscript critically for important intellectual content: JA Orkwis; AK Wolf; ZJ Mularczyk; A Bryan; CS Smith; M Krutko; L Esfandiari; GM Harris.

Declaration of competing interest

The authors declare that they have no known competing financial interests or personal relationships that could have appeared to influence the work reported in this paper.

Data availability

Data will be made available on request.

References

[1] K.R. Jessen, R. Mirsky, J. Physiol. (2016) 594.
[2] K.R. Jessen, R. Mirsky, A.C. Lloyd, Cold Spring Harb. Perspect. Biol. (2015) 7.
[3] A. Kumar, H. Kaur, A. Singh, Pharmacol. Rep. (2018) 70.
[4] B.-S. Kim, J.J. Yoo, A. Atala, J. Biomed. Mater. Res. 68A (2004) 201–209.
[5] A.A. Al-Majed, T.M. Brushart, T. Gordon, Eur. J. Neurosci. 12 (2000) 4381.
[6] M.T. Chorsi, E.J. Curry, H.T. Chorsi, R. Das, J. Baroody, P.K. Purohit, H. Ilies, T. D. Nguyen, Adv. Mater. (2019) 31.
[7] E. Fukada, I. Yasuda, Jpn. J. Appl. Phys. 3 (1964) 117.
[8] J.A. Orkwis, A.K. Wolf, S.M. Shahid, C. Smith, L. Esfandiari, G.M. Harris, Macromol. Biosci. 20 (2020), 2000197.
[9] T. Lei, L. Yu, G. Zheng, L. Wang, D. Wu, D. Sun, J. Mater. Sci. 50 (2015) 4342.
[10] S. Politi, F. Carotenuto, A. Rinaldi, P.Di Nardo, V. Manzari, M.C. Albertini, R. Araneo, S. Ramakrishna, L. Teodori, Nanomaterials (Basel) 10 (2020).
[11] G.M. Harris, N.N. Madigan, K.Z. Lancaster, L.W. Enquist, A.J. Windebank, J. Schwartz, J.E. Schwarzbauer, Matrix Biol. (2017) 60–61.
[12] G.M. Harris, I. Raitman, J.E. Schwarzbauer, Methods Cell Biol. (2018) 143.
[13] Z. Xu, J.A. Orkwis, B.M. DeVine, G.M. Harris, J. Tissue Eng. Regener. Med. (2020) 14.
[14] Z. Xu, J.A. Orkwis, G.M. Harris, Int. J. Mol. Sci. (2021) 22.
[15] K.R. Jessen, R. Mirsky, Front. Cell. Neurosci. (2019) 13.
[16] A.N. Koppes, A.L. Nordberg, G.M. Paolillo, N.M. Goodsell, H.A. Darwish, L. Zhang, D.M. Thompson, Tissue Eng. Part A (2014) 20.
[17] A.N. Koppes, N.W. Zaccor, C.J. Rivet, L.A. Williams, J.M. Piselli, R.J. Gilbert, D. M. Thompson, J. Neural Eng. (2014) 11.
[18] Z. Liang, T. Lei, S. Wang, Z. Luo, X. Hu, BioTechniques (2019) 67.
[19] L.E. Kokai, Y.C. Lin, N.M. Oyster, K.G. Marra, Acta Biomater. (2009) 5.
[20] C.A. Schneider, W.S. Rasband, K.W. Eliceiri, Nat. Methods 9 (2012) 671.
[21] P.-S. Liao, T.-S. Chen, P.-C. Chung, J. Inf. Sci. Eng. 17 (2001) 713.
[22] P. Martins, A.C. Lopes, S. Lanceros-Mendez, Prog. Polym. Sci. 39 (2014) 683.
[23] J. Bruton, in: J. Bruton (Ed.), Building a Lower-power Linear Actuator with Arduino | James Bruton 38, YouTube, 2018, p. 20.
[24] D.O. Freytes, J. Martin, S.S. Velankar, A.S. Lee, S.F. Badylak, Biomaterials (2008) 29.
[25] J. van Meerloo, G.J.L. Kaspers, J. Cloos, Cell sensitivity assays: the MTT assay, in: I. A. Cree (Ed.), Cancer Cell Culture: Methods and Protocols, Humana Press, Totowa, NJ, 2011, p. 237.
[26] C. Chang, V.H. Tran, J. Wang, Y.K. Fuh, L. Lin, Nano Lett. (2010) 10.
[27] A. Wang, M. Hu, L. Zhou, X. Qiang, Nanomaterials (Basel) 9 (2019).
[28] K. Tashiro, M. Kobayashi, H. Tadokoro, E. Fukada, Macromolecules 13 (1980) 691.
[29] J.J. Stankus, J. Guan, K. Fujimoto, W.R. Wagner, Biomaterials (2006) 27.
[30] G.E. Rutkowski, C.A. Heath, Biotechnol. Prog. 18 (2002) 362.
[31] Y. Mao, J.E. Schwarzbauer, Matrix Biol. (2005) 24.
[32] I. Wierzbicka-Patynowski, Y. Mao, J.E. Schwarzbauer, Curr Protoc Cell Biol 25 (2004) 10.12.1–10.12.10.
[33] P.J. Arthur-Farraj, M. Latouche, D.K. Wilton, S. Quintes, E. Chabrol, A. Banerjee, A. Woodhoo, B. Jenkins, M. Rahman, M. Turmaine, G.K. Wicher, R. Mitter, L. Greensmith, A. Behrens, G. Raivich, R. Mirsky, K.R. Jessen, Neuron (2012) 75.
[34] T. Lei, X. Cai, X. Wang, L. Yu, X. Hu, G. Zheng, W. Lv, L. Wang, D. Wu, D. Sun, L. Lin, RSC Adv. 3 (2013) 24952.
[35] R. Gregorio, J. Appl. Polym. Sci. 100 (2006) 3272.
[36] N. Weber, Y.S. Lee, S. Shanmugasundaram, M. Jaffe, T.L. Arinzeh, Acta Biomater. (2010) 6.
[37] E. Fukada, I. Yasuda, J. Phys. Soc. Jpn. 12 (1957) 1158.

[38] N.-H. Zhang, IEEE Trans. Dielectr. Electr. Insul. 22 (2014) 1376.
[39] J. Nunes-Pereira, V. Sencadas, V. Correia, J.G. Rocha, S. Lanceros-Méndez, Sensors Actuators A Phys. 196 (2013) 55.
[40] D.S. Cooney, E.G. Wimmers, Z. Ibrahim, J. Grahammer, J.M. Christensen, G. A. Brat, L.W. Wu, K.A. Sarhane, J. Lopez, C. Wallner, G.J. Furtmuller, N. Yuan, J. Pang, K. Sarkar, W.P. Lee, G. Brandacher, Sci. Rep. (2016) 6.
[41] D. Jeong, J. Lee, Y.S. Yi, Y. Yang, K.W. Kim, J.Y. Cho, Mediat. Inflamm. (2013) 2013.
[42] L. Persano, C. Dagdeviren, Y. Su, Y. Zhang, S. Girardo, D. Pisignano, Y. Huang, J. A. Rogers, Nat. Commun. (2013) 4.
[43] Y. Qian, Y. Cheng, J. Cai, X. Zhao, Y. Ouyang, W.-E. Yuan, C. Fan, Regen. Med. (2019) 14.
[44] O. Gryshkov, F. Al Halabi, A.I. Kuhn, S. Leal-Marin, L.J. Freund, M. Förthmann, N. Meier, S.-A. Barker, K. Haastert-Talini, B. Glasmacher, Int. J. Mol. Sci. 22 (2021).
[45] L.T. Beringer, X. Xu, W. Shih, W.-H. Shih, R. Habas, C.L. Schauer, Sensors Actuators A Phys. 222 (2015) 293.
[46] D.J. Heredia, C. De Angeli, C. Fedi, T.W. Gould, Neurosci. Lett. (2020) 729.
[47] N. Adadi, M. Yadid, I. Gal, M. Asulin, R. Feiner, R. Edri, T. Dvir, Adv. Mater. Technol. 5 (2020) 1900820.
[48] I. Manabe, T. Shindo, R. Nagai, Circ. Res. (2002) 91.
[49] J. Huang, Z. Ye, X. Hu, L. Lu, Z. Luo, Glia (2010) 58.
[50] H. Xu, Y. Yan, S. Li, Biomaterials (2011) 32.
[51] A. Sadeghi, F. Moztarzadeh, J. Aghazadeh Mohandesi, Int. J. Biol. Macromol. 121 (2019).
[52] L. Wang, Y. Wu, T. Hu, B. Guo, P.X. Ma, Acta Biomater. (2017) 59.
[53] S. Wu, Y. Qi, W. Shi, M. Kuss, S. Chen, B. Duan, Acta Biomater. (2022) 139.
[54] Y. Wu, L. Wang, B. Guo, Y. Shao, P.X. Ma, Biomaterials (2016) 87.
[55] Y. Wu, L. Wang, T. Hu, P.X. Ma, B. Guo, J. Colloid Interface Sci. (2018) 518.
[56] J.S. Taras, S.M. Jacoby, Tech. Hand Up. Extrem. Surg. (2008) 12.
[57] V. Chiono, C. Tonda-Turo, Prog. Neurobiol. (2015) 131.
[58] D. Arslantunali, T. Dursun, D. Yucel, N. Hasirci, V. Hasirci, Med. Devices (Auckl) 7 (2014).
[59] Y. Qian, Y. Cheng, J. Song, Y. Xu, W.E. Yuan, C. Fan, X. Zheng, Small (2020) 16.
[60] N. Abzan, M. Kharaziha, S. Labbaf, Mater. Des. 167 (2019), 107636.
[61] Q.L. Loh, C. Choong, Tissue Eng. Part B Rev. (2013) 19.
[62] V. Karageorgiou, D. Kaplan, Biomaterials (2005) 26.
[63] X. Wen, P.A. Tresco, Biomaterials (2006) 27.
[64] A.J. Engler, S. Sen, H.L. Sweeney, D.E. Discher, Cell (2006) 126.
[65] G.M. Harris, M.E. Piroli, E. Jabbarzadeh, Adv. Funct. Mater. (2014) 24.
[66] T.M. Dinis, R. Elia, G. Vidal, Q. Dermigny, C. Denoeud, D.L. Kaplan, C. Egles, F. Marin, J. Mech. Behav. Biomed. Mater. (2015) 41.
[67] G. Liu, Q. Zhang, Y. Jin, Z. Gao, Neural Regen. Res. (2012) 7.
[68] Y. Cheng, Y. Xu, Y. Qian, X. Chen, Y.M. Ouyang, W.E. Yuan, Nano Energy (2020) 69.
[69] T.H. Barker, Biomaterials (2011) 32.
[70] E. Cady, J.A. Orkwis, R. Weaver, L. Conlin, N.N. Madigan, G.M. Harris, Bioengineering (Basel) 7 (2020).
[71] W.P. Daley, K.M. Yamada, Curr. Opin. Genet. Dev. (2013) 23.
[72] M. Idini, P. Wieringa, S. Rocchiccioli, G. Nieddu, N. Ucciferri, M. Formato, A. Lepedda, L. Moroni, Acta Biomater. (2019) 96.
[73] M. Nune, M. Bhat, A. Nagarajan, J. Med. Biol. Eng. (2022) 42.
[74] J.A. Gomez-Sanchez, K.S. Pilch, M. van der Lans, S.V. Fazal, C. Benito, L. J. Wagstaff, R. Mirsky, K.R. Jessen, J. Neurosci. (2017) 37.